CrystEngComm

ROYAL SOCIETY OF CHEMISTRY

PAPER

View Article Online
View Journal

Cite this: DOI: 10.1039/d6ce00012f

In situ transmission electron microscopy observations of $CaCO_3$ crystallization onto polysaccharide-coated nanoparticles

Brenna M. Knight, [ab] Biao Jin, [c] Yuna Bae, [c] James J. De Yoreo [cd] and Patricia M. Dove *[abef]

Polysaccharides and proteoglycans are widely associated with the organic matrix at sites of $CaCO_3$ biomineralization, and previous studies indicate that these macromolecules may confer greater roles in mineral nucleation than previously recognized. This investigation uses *in situ* liquid-phase transmission electron microscopy (LP-TEM) to observe $CaCO_3$ nucleation onto aminated silica (SiO_2–NH_3^+) nanoparticles treated with a layer of chitosan (near-neutral derivative of chitin) or heparin (a carboxylated and highly sulfated glycosaminoglycan). In the absence of polysaccharides, few $CaCO_3$ particles formed and exhibited mobility. However, the SiO_2–NH_3^+ nanoparticles were enveloped in a region of higher mass density relative to the bulk solution, suggesting the development of a local solute-rich environment that surrounds the charged NH_3^+ groups. The heparin- or chitosan-coated silica particles also exhibited regions of higher mass density around the nanoparticles. In the presence of these polysaccharide coatings, we observed the nucleation of abundant $CaCO_3$ particles whereby the polyanionic heparin promoted more nucleation than the weakly cationic chitosan. Many crystallites appeared to form at the polysaccharide–TEM cell membrane–solution interface, further indicating interfacial and macromolecule-specific control on crystallization. The combined results demonstrate that chitosan and heparin have an appreciable effect on the timing, size, and location of $CaCO_3$ nucleation compared to the polysaccharide-free nanoparticles.

Received 6th January 2026,
Accepted 18th March 2026

DOI: 10.1039/d6ce00012f

rsc.li/crystengcomm

1. Introduction

During biological crystallization, the organic matrix modulates the timing and placement of biominerals to form unique biocomposites. Macromolecules confer much of this activity.[1–6] In $CaCO_3$-forming systems, the organic matrix often contains chitin and anionic biopolymers (*e.g.*, SO_3^- and/or COO^- functionalized) alongside specialized proteins.[1,7–13] However, a mechanistic understanding of how macromolecular properties translate to control over $CaCO_3$ nucleation and subsequent growth and phase transformation processes is not yet resolved. Insight into where and how $CaCO_3$ nucleation occurs within organic interfacial environments is also relevant to subsurface and engineered systems, where nanoscale interphases associated with organic matter and mineral surfaces can influence carbonate scaling and the co-precipitation of critical rare earth elements.

Investigations of $CaCO_3$ nucleation onto chitosan materials with varied degrees of sulfation demonstrated a relationship between net charge, the position of functional groups, calcium binding, and interfacial free energy (γ_{net}).[14,15] Parallel molecular dynamics (MD) studies predict that Ca^{2+} interactions with sulfated chitosans are solvent-separated by distances that correlate with the degree of sulfation (0.5–1.2 nm).[15–20] Model results also indicate that nucleation is favored to occur at a distance from the polysaccharide–water interface that correlates with the position of solvation waters around functional groups and Ca^{2+}.[15,16,18] The concept that crystal nucleation can occur away from a surface, but within the non-bulk diffuse layer, is supported by recent studies using liquid phase *in situ* transmission electron microscopy (LP-TEM). For example, an investigation of $CaCO_3$ nucleation onto carboxyl-rich *de novo* protein templates reported an ≈1 nm separation between nanocrystals and the protein substrate.[21] This distance is consistent with the thickness of the hydration layer around calcite,[21,22] further implicating solvation as a control on nucleation. Also, an ≈1 nm separation was observed between new nuclei and existing particles in TEM studies of colloidal

[a] *Department of Chemistry, Virginia Tech, Blacksburg, VA 24061, USA. E-mail: dove@vt.edu*
[b] *Macromolecules Innovation Institute, Virginia Tech, Blacksburg, VA 24061, USA*
[c] *Physical Sciences Division, Pacific Northwest National Laboratory, Richland, WA 99354, USA*
[d] *Department of Materials Science and Engineering, University of Washington, Seattle, WA 98195, USA*
[e] *Department of Geosciences, Virginia Tech, Blacksburg, VA 24061, USA*
[f] *Department of Materials Science and Engineering, Virginia Tech, Blacksburg, VA 24061, USA*

gold[23] and hematite.[24] These experimental and computational lines of evidence raise the question of where $CaCO_3$ nucleation occurs within the substrate–solution interfacial environment for polysaccharides such as chitosan. Using insights from our previous experimental and modeling studies of calcite nucleation onto sulfated and uncharged polysaccharides, we hypothesize that $CaCO_3$ nucleation takes place away from the polysaccharide surface at a separation distance that is dependent on macromolecular and solution properties in the interphase region/diffuse layer.

To test this hypothesis, we used *in situ* LP-TEM to image real-time nucleation of $CaCO_3$ in the presence of the polysaccharides. The technique allows observations of crystallization processes at the nanometer to near-Å scale.[25,26] However, biomacromolecules are difficult to image by this approach because of their low electron density,[27–29] and therefore, they present little contrast between the molecule and the adjacent bulk solution. The low contrast is exacerbated by the variable interphase region between the bulk solution and the polysaccharide. The nature of this region is dependent on solution composition (*e.g.*, pH and ionic strength) as well as biopolymer properties that include net charge, charge geometry/configuration, and persistence length (*i.e.*, effective chain stiffness).[30–32] We were able to address some of the limitations by utilizing 20 nm aminated silica nanoparticles (SiO_2–NH_3^+) as substrates for the polysaccharides (Fig. 1A and inset). By this approach, the silica–PS interface was better resolved in the TEM cell.

The experiments were designed to observe nucleation in calcite-supersaturated solutions containing: (1) SiO_2–NH_3^+ nanoparticles (nps); (2) SiO_2–NH_3^+ nps treated to have a chitosan coating; and (3) SiO_2–NH_3^+ nps treated with heparin. The chitosan and heparin polysaccharides were chosen as models to represent macromolecules in the organic matrix that present near-neutral (to slightly cationic) and high net charge functional groups, respectively.

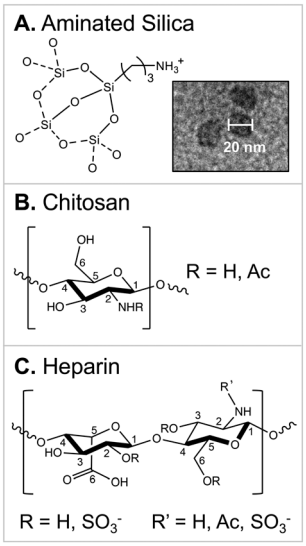

Fig. 1 Materials used in this study. (A) Aminated silica nanoparticles (20 nm) were used as a control and subsequently coated with polysaccharides; (B) chitosan; (C) heparin.

2. Experimental

2.1. Materials

The untreated SiO_2–NH_3^+ nps (Fig. 1A, 20 nm, nanoComposix) were used as a control relative to the polysaccharide-coated materials. Each silica amine has a +1 charge (pK_a ≈9–11) at the experimental pH (6.9–7.6) of this study.[33] This high net-positive charge corresponds to approximately 2 NH_3^+ groups per nm^2.[34]

The polysaccharide compositions were as follows. Chitosan (Fig. 1B, sourced from Millipore Sigma, medium molecular weight, 270 kDa (ref. 15)) is a chitin derivative in which a fraction of the acetyl groups is converted to free amines. Chitosan presents an interfacial environment with a relatively low charge density, some hydrogen bonding, and thus a relatively short persistence length (Kuhn length).[30] Given that these properties govern how polymers occupy the interfacial region between the solution and substrate, this material has a greater conformational freedom (relative to heparin) and can be considered a weakly flexible biopolymer. The material had a degree of deacetylation/degree of amination = 0.76 (by ^1H NMR[15]) and an amine charge = +0.06 to +0.22 at pH 6.9–7.6 ($pK_{a,chitosan}$ ≈6.5).[35,36] Therefore, the average charge per monosaccharide on chitosan was ≈+0.05 to +0.17. Assuming a surface area that is approximately equal to a glucose repeat unit, we estimate that chitosan presents a low net positive charge of ≈+0.04–0.13 charged amines per nm^2.

In contrast, heparin (Fig. 1C, sourced from Millipore Sigma, one COO^- and 2.4 SO_3^- groups per disaccharide, 18 kDa (ref. 37)) is a highly charged, polyanionic polysaccharide containing both carboxyl and sulfate groups. Each group has a −1 charge at the experimental pH ($pK_{a,heparin}$ ≈3–5),[37–39] corresponding to an average charge of −1.7 per monosaccharide for our material, or approximately 1.3 anionic groups per nm^2 (based on a glucose repeat unit). Heparin thereby presents a stronger electrostatic repulsion between chains and thus a larger persistence length to behave as a semi-rigid polyelectrolyte.[30]

2.2. Nanoparticle coating

For each experiment, SiO_2–NH_3^+ nanoparticles were coated with chitosan or heparin using crosslinking (XL) methods adapted for sulfated chitosan derivatives.[15,40,41] Briefly, heparin and chitosan solutions (2 mg mL^{-1}) were prepared in deionized (DI) water and DI water containing 1% v/v acetic acid, respectively. Glutaraldehyde (1% in DI water, 0.25 mL) was added to the polysaccharide solutions (0.5 mL). After 20 min, aminated silica nanoparticles (0.25 mL, 2 mg mL^{-1} in DI water) were added. The mixtures were sonicated for 15 min and then centrifuged (10 min, 7000 rpm) and washed with DI water 3 times. Solutions were sonicated for 5 min prior to each use. Attenuated total reflectance (ATR, Bruker Alpha II, resolution 2 cm^{-1}, 32 scans, 4000–6000 cm^{-1}) was

used to confirm that polysaccharides were attached to the aminated silica nanoparticles (Fig. S1).

2.3. Liquid-phase transmission electron microscopy (LP-TEM)

The *in situ* crystallization observations used an experimental setup that was modeled after the method employed by Davila-Hernandez *et al.*[21] The liquid-cell contained two square silicon chips (Hummingbird Scientific) measuring 2.6 × 2.6 mm^2 each containing 50 nm-thick silicon nitride (Si_3N_4) membranes with 50 × 200 μm^2 imaging windows. Prior to use, the chips underwent a 2 min plasma cleaning process with a Harrick Plasma Cleaner. For a typical experiment, 0.5 μL of 10 mM $CaCl_2$ and 0.1 μL 2% nanoparticle solution were applied to the spacer chip with a spacer thickness of 100 nm. Next, 0.5 μL of a 10 mM $NaHCO_3$ solution was added to produce a supersaturated $CaCO_3$ solution (supersaturation (σ) with respect to calcite ($\sigma_{calcite}$) ≈1.6),[42,43] and the reaction solution was sealed using a window chip to form a liquid-cell. The liquid-cell was then placed inside a Hummingbird Scientific sample holder. A leak check was conducted by inserting the assembled holder into a Hummingbird Scientific high-vacuum leak checking station for 2 min. This station features a low base pressure ($<1 \times 10^{-6}$ mbar) and short pumping and venting times, and allows the liquid-cell window to be imaged with optical microscopy. The holder was then inserted into an FEI (a subsidiary of Thermo Fisher Scientific) Titan Environmental TEM operated at 300 kV with a Gatan UltraScan 1000 camera.

A series of TEM images were captured beginning ≈10 min after mixing using an Eagle CCD with a resolution of 1024 × 1024 pixels, a condenser aperture size of 50 μm, and a spot size of 3 nm. *In situ* movies were recorded using the free software Gatan DigitalMicrograph and post-processing of images from the movies was performed using the open-source software ImageJ.[44] A low electron dose rate of ≈100 $e^- nm^{-2} s^{-1}$ was employed to minimize beam effects. A schematic of the TEM setup is shown in Fig. S2.

For additional control experiments of 2% aminated SiO_2 nanoparticles in pure water (without solute ions) and at pH 9 ($\sigma_{calcite}$ ≈1.6, 2.5 mM $CaCl_2$ and 1 mM Na_2CO_3), LP-TEM was performed using an Insight Chips® nanochannel holder. This holder featured a 130 nm channel height, with inner surfaces encapsulated by 25 nm-thick silicon nitride and coated with Al_2O_3. The solution was loaded into the nanochannel *via* a flow line. Imaging was conducted with a Gatan Metro 300 camera.

3. Results and discussion

For all *in situ* systems, the $CaCO_3$ products that formed are expected to be crystalline. Selected area electron diffraction (SAED) could not discern if the particles were crystalline or amorphous materials (Fig. S3). However, the nucleating particles were significantly more electron dense (*i.e.*, darker) than would be expected for a hydrated cluster or amorphous material.[45–47]

Particles were observed in regions that were different from the initial location of the electron beam, indicating that beam effects were not driving the nucleation process.[21] Moreover, as discussed below, each of the three types of particles used in the study gave material-specific results. Thus, the progression of nucleation, both the location and rate, was not determined by solution radiolysis. Representative images from each experiment are shown in Fig. 2.

In $CaCO_3$ supersaturated solutions, the aminated SiO_2 nanoparticles (control) were enveloped in a region of solution that was darker than that of the surrounding bulk solution (outlined in white in Fig. 2B). This region presented an average width of 16 nm as measured from the nanoparticle surface to its perimeter (*e.g.*, Fig. 2B; the distance between the yellow and white lines) with a maximum lateral extent of 34 nm (*e.g.*, shaded area in Fig. 4A). All distances were determined by applying the measurement tool in ImageJ[44] to

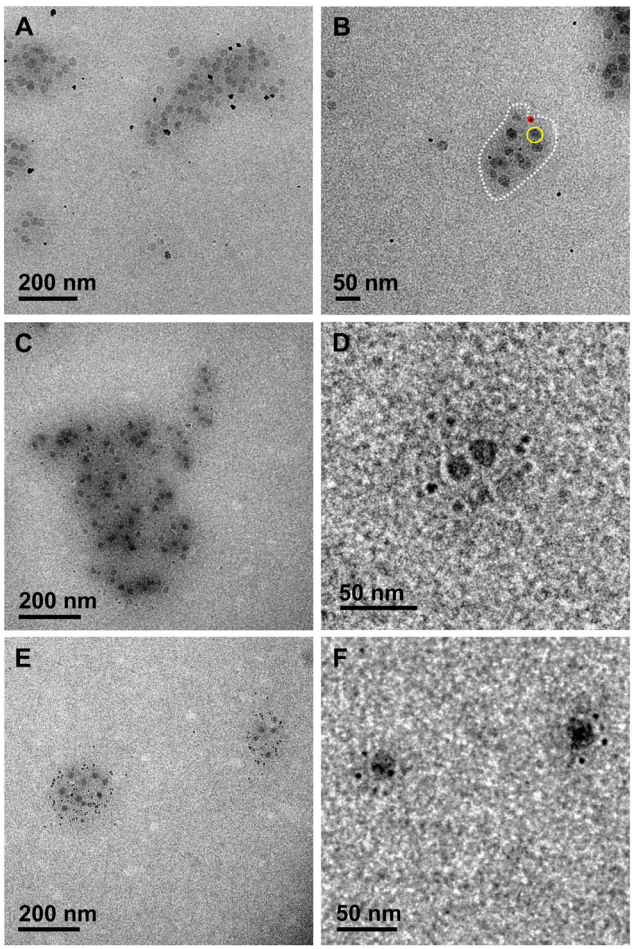

Fig. 2 *In situ* LP-TEM images of $CaCO_3$ crystallites that formed in the absence and presence of polysaccharides at t ≈10 min after initial nucleation. (A and B) SiO_2–NH_3^+ nanoparticles alone (control). Panel B highlights relevant features; larger, dark gray round features are the SiO_2 spherical nanoparticles (yellow), and smaller dark spots are $CaCO_3$ (red). The region surrounding the nanoparticle of higher mass density than the bulk solution is outlined in white. (C and D) Chitosan-treated SiO_2–NH_3^+ nanoparticles. (E and F) Heparin-treated SiO_2–NH_3^+ nanoparticles. E and F are from the heparin 3 replication (*e.g.* Fig. 4E and 5E). Representative images from each heparin experiment are shown in Fig. S4.

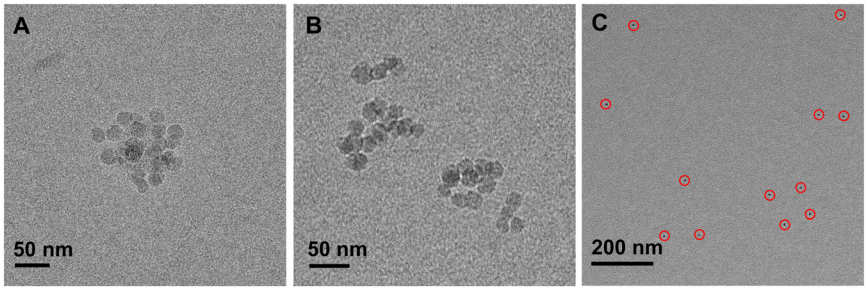

Fig. 3 *In situ* LP-TEM images of aminated silica nanoparticles demonstrate that the mass density surrounding the nps and the bulk solution are similar in (A) distilled, deionized H_2O; (B) a calcite-supersaturated solution at the higher pH 9 (amines are uncharged). (C) $CaCO_3$ particles (red) are nucleated in the bulk solution when the np amines are uncharged.

the collected images. The increased grayscale value in this region reflects a greater mass density relative to the bulk solution composition and, thus, is indicative of ion accumulation around the charged NH_3^+ groups, creating a solute-rich environment. To confirm this interpretation, we conducted additional control experiments in water (without solute ions) (Fig. 3A) and did not find a darker region around the nanoparticle. This was also true for another experiment using calcite-supersaturated solutions at pH 9 (where the amines are uncharged) (Fig. 3B). In these solutions, $CaCO_3$ crystallites formed in the bulk solution without evidence of np association (Fig. 3C). An implication of these observations is that substrate charge, including simple aminated SiO_2 nanoparticles without a biopolymer treatment, can facilitate locally higher ion concentrations, and thus a potentially greater driving force for $CaCO_3$ nucleation.

Returning to the polysaccharide-free control experiments (Fig. 2A and B), the induction time to the first appearance of $CaCO_3$ crystals was ≈40 min. The induction time was measured as the period of time between the addition of

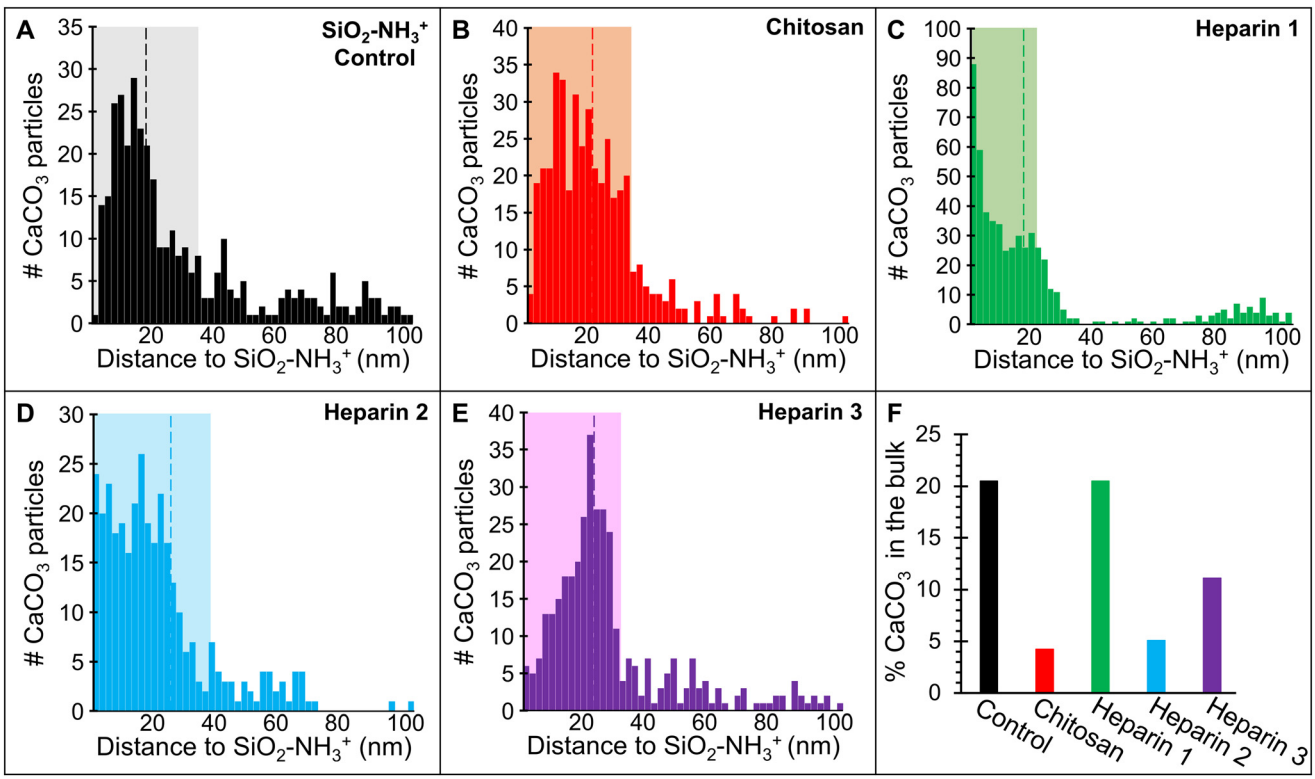

Fig. 4 Measured distance from the outer edge of a $CaCO_3$ crystal to the outer edge of the nearest, visible SiO_2–NH_3^+ nanoparticle (up to 100 nm) for (A) control/SiO_2–NH_3^+, (B) chitosan-XL-SiO_2–NH_3^+, and (C–E) three trials of heparin-XL-SiO_2–NH_3^+. Each bar represents a 2 nm range. Shaded regions denote the thickness of the electron dense 'cloud' surrounding the SiO_2–NH_3^+ particles and dotted lines denote the average cloud thickness. (F) % of $CaCO_3$ particles that nucleated in the bulk. Three trials were performed with heparin because, during the first two, nucleation had already occurred by the time imaging began. Consequently, in order to ensure that the calcium carbonate particles were not moving between the time of nucleation and imaging, a third trial was carried out during which the initial nucleation events were successfully captured.

$NaHCO_3$ to the TEM cell (*i.e.*, when the solution was first supersaturated, sect. 2.3) and observation of the initial $CaCO_3$ particles. Crystals formed in the bulk solution as well as near the SiO_2 nanoparticles. At ≈10 min post-induction, aggregates and larger individual crystals of $CaCO_3$ were observed near the nanoparticles, and smaller crystals formed in the bulk solution (Fig. 2A and B). By measuring the distance from the outer edge of each SiO_2–NH_3^+ nanoparticle to the nearest edge of each $CaCO_3$ crystal (*e.g.*, Fig. 2B; between the yellow and red circles), we determined that most nucleation occurred within 30 nm of the SiO_2–NH_3^+ surface, which was similar to the estimated thickness of the electron-dense zone (Fig. 4A). Away from the nanoparticles, a significant number of $CaCO_3$ particles (≈21%) formed in the bulk solution. However, many of these particles exhibited mobility during the first stages of nucleation.

The average diameter of particles formed in the SiO_2–NH_3^+ control experiment was 7.7 ± 3.8 nm; however, the crystal size distribution was asymmetric with a significant tail extending to larger sizes (Fig. 5A). Many particles grew to a diameter >15 nm (and up to 31 nm). There was no apparent association between particle size and distance from the nanoparticle edge. The low ratio (1 : 4) of the total number of $CaCO_3$ crystals to the number of silica nanoparticles within a representative viewing area indicates that the control SiO_2–NH_3^+ particles and the associated zone do not have a strong direct nucleation ability relative to the bulk solution (Fig. 5F). This is further supported by *in situ* observations that the $CaCO_3$ crystals were in motion during and after their formation, indicating that they were not bound to the aminated silica nanoparticles.

Quantifying the position of $CaCO_3$ crystals relative to the polysaccharide coating in the TEM liquid-cell presented challenges because the polysaccharides have a low mass density, which limited our ability to directly measure the thickness of the coating. Hence, we could not readily resolve the exact position of the crystallites relative to the polysaccharide–solution interface. The difficulty was amplified because TEM images are 2-dimensional projections of 3-dimensional features such that: 1) some distance measurements will be biased to apparent values that are smaller than the actual; 2) the measurements cannot discern the true distance of particles with positions above or overlapping the SiO_2–NH_3^+ nanoparticles. However, the images of the polysaccharide-coated nanoparticle systems (Fig. 2C–F) show significant contrast between the $CaCO_3$ particle-dense regions near nanoparticles and the particle-free bulk relative to the control (Fig. 2A and B). By assuming that this higher mass density region corresponds to the polysaccharide coating or interphase region and the associated ions (shaded regions in Fig. 4B–E), we were able to obtain insight into where crystals nucleated. We measured the distance from the nearest edge of each $CaCO_3$ crystal to the outer edge of

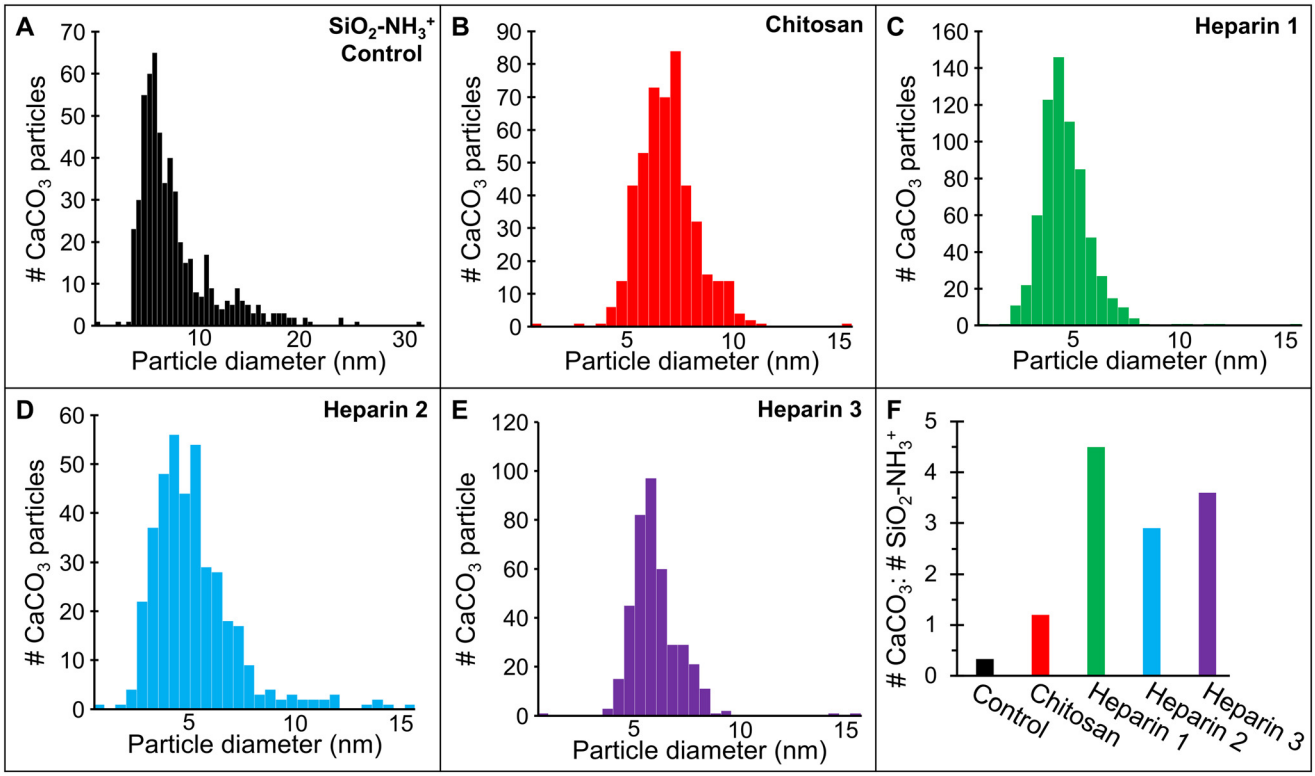

Fig. 5 Measured $CaCO_3$ crystal diameters for (A) the control as SiO_2–NH_3^+ nanoparticles, (B) chitosan-XL-SiO_2–NH_3^+, and (C–E) three replications of heparin-XL-SiO_2–NH_3^+. Only the control system had $CaCO_3$ particles with diameters >15 nm. Each bar represents a bin size of 0.5 nm and notes variable *y*-axis ranges for panels A–E. (F) Particle number density expressed as the number of $CaCO_3$ particles per SiO_2–NH_3^+ particles.

each SiO_2–NH_3^+ nanoparticle. Most nucleation occurred <30 nm from the SiO_2–NH_3^+ surface (Fig. 4B), which was within the estimated width of the electron-dense region and is comparable to that seen for the control.

In contrast to the control, with the chitosan-coated nanoparticles, most (96%) $CaCO_3$ particles nucleated in close association with the polysaccharide interfacial region while very few crystals formed in the bulk solution (Fig. 2C and D and 4B and F). Moreover, the induction time to crystallization (≈25–30 min) was significantly shorter than for the control experiments. Also, the resulting $CaCO_3$ particles were stationary, indicating they were at least weakly bound to the polysaccharide. Under these conditions, $CaCO_3$ crystals formed with a higher number density, averaging 1.2 $CaCO_3$ per SiO_2–NH_3^+ nanoparticle (Fig. 5F) and a smaller average particle size with a narrower range of diameters (6.4 ± 1.3 nm, Fig. 5B) compared to the control, though the peak in the size distribution was similar for both. Few to no aggregates of $CaCO_3$ crystals were observed.

Like chitosan, most $CaCO_3$ crystals preferentially formed near the heparin-coated nanoparticles (80–95%) with a few in the bulk solution and they appeared at still-shorter incubation times (≈20 min) (Fig. 2E and F and 4C–F and S4). Compared to the chitosan-coated and control experiments, the number of heparin-associated $CaCO_3$ crystals was the greatest with an average of 2.9 crystallites per SiO_2–NH_3^+ nanoparticle (Fig. 5F). The average crystal size was smaller (diameters = 4.0 ± 1.2, 4.7 ± 2.0, and 5.4 ± 1.1 nm (Fig. 5C–E, respectively)) with an overall average of 4.6 ± 1.5 nm. These diameters are near or within estimates for the calcite critical nucleus size (1–5 nm) for the estimated supersaturation conditions of these experiments.[22,48]

A relationship between the particle size and distance from the SiO_2–NH_3^+ particle edge was not observed for the heparin or chitosan experiments. Note that the three heparin trials resulted in 'clouds' of variable thicknesses around the nps, which roughly correlated with the distributions of the $CaCO_3$ crystals. This suggests that heterogeneities in the thickness of heparin coating and/or the interphase environment were the primary influence on measured $CaCO_3$ distances (*e.g.*, Fig. 4C–E).

The smaller particle sizes, higher particle numbers, and shorter induction times measured for the chitosan and heparin systems are consistent with previous optical observations of $CaCO_3$ crystallization in the presence of polymer additives, particularly with the addition of anionic molecules (*e.g.*, carboxymethyl chitosan).[49–51] The results are also consistent with rate measurements that determined that the kinetic term of the rate expression increases with the net charge of the polysaccharide (Fig. S5).[14,15] However, it is important to remember that crystal size differences could be rooted in nucleation and/or extent of growth. Observations from this study cannot fully resolve the relative contributions between polysaccharide effects on growth rate *versus* nucleation. Hence, an alternative explanation is that the smaller particles may be a consequence of slower growth due to a post-nucleation reduction in supersaturation.

Recognizing the limitations of our measurements for the distance of separation between the $CaCO_3$ crystals and SiO_2–NH_3^+ nanoparticles, we propose that nucleation occurs in two types of environments. First, the interfacial environment within 0–40 nm from the nanoparticle surface has the primary control on crystal nucleation. Second, at distances beyond ≈40 nm, nucleation is dominated by bulk solution properties.

We acknowledge it is unlikely that the aminated silica nanoparticles alone (control) could regulate crystallization at distances of up to ≈20 nm into the solution. The Debye length for interfaces around these materials is expected to be <5 nm,[52] suggesting that observed long-range effects may be a result of collective properties of the materials and solution environment rather than individual molecular level forces. This is consistent with the idea that $CaCO_3$ nucleation is driven by water restructuring during substrate–ion interactions (*i.e.*, entropically dominated) as opposed to coulombic forces alone.[53–55] However, we observed a maximum number of $CaCO_3$ particles at distances of 12–14 nm from a nanoparticle edge, which is well beyond the length that surfaces generate structured hydration layers (typically <2 nm as seen by 3D atomic force microscopy).[56–59] Moreover, our value is much larger than those reported or predicted by molecular dynamics for other nucleating systems (1–2 nm).[15,16,21,23,24]

Consequently, appealing to a decrease in the interfacial energy due to such structuring as a source of enhanced nucleation is unfounded. Similarly, although electric fields can introduce an additional term in the work of cluster formation that reduces the critical size and thus increases nucleation rates,[60] the distances from the functionalized particle surfaces and large ion concentrations would seem to preclude this effect as a source of enhanced nucleation. Further investigation will be required, but even if the heterogeneous distributions of Ca^{2+} and CO_3^{2-} are such that their individual chemical potentials are uniform throughout the solution, perhaps small increases in the product of Ca^{2+} and CO_3^{2-} activities lead to a consequent increase in local supersaturation that promotes nucleation in the solution near these nanoparticles (*i.e.*, homogeneous nucleation).[13,61–65]

Irrespective of the mechanism, the larger number density of $CaCO_3$ crystals that form in the region of the polysaccharide-coated nps compared to the bulk solution and the control experiments indicates the biopolymer-specific interactions with ions to promote nucleation. It is plausible that the greater persistence length of the heparin, which behaves as a semi-rigid polyelectrolyte, particularly under the low ionic strength conditions of these experiments,[32,66] presents greater spatial organization with extended chains and thus more stable binding sites. The result is local environments that favor Ca^{2+} and HCO_3^- ion-rich regions and increase the probability of forming $CaCO_3$ critical nuclei

(*e.g.*, ref. 15). This interpretation is consistent with our observations of shorter induction times, greater nucleation density, and similar distances between the crystallites and np surface. However, the variable $CaCO_3$ particle distributions between samples (*e.g.*, Fig. 4C–E) prevent a firm conclusion.

Chitosan, with its low charge and thus greater flexibility and shorter effective persistence length,[31] presents a less-organized interphase region. Although this study could not resolve the structure and properties of the region, it is plausible that binding sites are weaker with greater fluctuations, resulting in fewer nucleation events compared to heparin. However, our study cannot assess if the origins of these effects on $CaCO_3$ nucleation are kinetic (*e.g.*, the number of possible nucleation sites,[67] attachment rates, and barriers to ion binding, such as the desolvation barrier[64]) and/or thermodynamic (*e.g.*, the supersaturation and interfacial free energy of forming a new crystal (γ_{net})). Both polysaccharides, however, yield favorable environments for nucleation near the polysaccharide–solution interface relative to the bulk solution.

The *in situ* TEM images also indicate that $CaCO_3$ crystals in the polysaccharide systems did not form directly on (*e.g.*, separation distance = 0 nm; Fig. 5) or above the SiO_2–NH_3^+ nps in the chitosan system, nor in two of the heparin replications. Rather, $CaCO_3$ appears to form in definitive rings around coated nanoparticles (Fig. 2C and F). This is notable because if $CaCO_3$ nucleates in an approximate hemisphere around the coated silica nps, the 2D projections would yield images of $CaCO_3$ crystals overlapping with the silica substrates at all distances. A plausible explanation for this observation is that $CaCO_3$ crystals nucleate near the boundary between the solution, the interphase region of polysaccharide coating, and the silicon nitride (Si_3N_4) membrane(s) that comprise the TEM liquid-cell. That is, crystals preferentially form at the polysaccharide–TEM membrane–solution interface. This scenario is supported by the fact that the particles do not undergo Brownian motion, implying that, like most objects imaged in liquid phase TEM, they exhibit greatly reduced mobility as a consequence of being in the vicinity of the membrane. Previous measurements show that γ_{net} for nucleating calcite is the largest for highly charged polysaccharides (*e.g.*, heparin).[14,15] This insight, combined with observations of the preferred crystal placements, would seem to suggest that introducing the TEM cell membrane to the polysaccharide–solution system reduces γ_{net} and/or increases the activity product or kinetic factors of the nucleation rate expression at the boundary of the materials (*i.e.*, at the polysaccharide–membrane–solution interface).

Observations in this study suggest a model for how polysaccharides influence the placement of $CaCO_3$ crystals during nucleation. Fig. 6 illustrates three types of interfaces in the TEM liquid-cell for our polysaccharide systems: 1) the Si_3N_4 membrane–solution interface that comprises the fluid *in situ* TEM cell, 2) polysaccharide–solution interface, and 3) polysaccharide–TEM membrane–solution interface. The γ_{net}, ion distributions, and kinetic factors for each system are thus a collective outcome of the associated interfaces.

Interface 1: Si_3N_4 membrane–solution. The Si_3N_4 membrane that comprises the upper and lower faces of the TEM cell is generally considered to be hydrophobic over a time scale that is similar to the short duration of our experiments (Fig. 6, interface 1). Weak interactions with water have a relatively low γ_{net} value for $CaCO_3$ formation, whereby crystallites displace H_2O to result in a favorable substrate for heterogeneous nucleation relative to nucleation in the bulk solution (homogeneous). However, the TEM cell membrane and solute ions also have weak interactions, leading to a low kinetic driver of crystal nucleation and few to no crystals forming at the Si_3N_4 membrane–solution interface as observed in this study (*e.g.*, Fig. 2C–F, lower right quadrants). In the SiO_2–NH_3^+ control system, particles moved after nucleating in the bulk (*i.e.*, away from nanoparticles), further suggesting little nucleation directly onto the Si_3N_4 membrane.

Interface 2: polysaccharide–solution. The interphase region between the hydrophilic polysaccharides and solution has a locally higher ion concentration compared to the bulk solution which, in turn, enhances water structuring (Fig. 6, interface 2). The degree of structure is dependent on specific

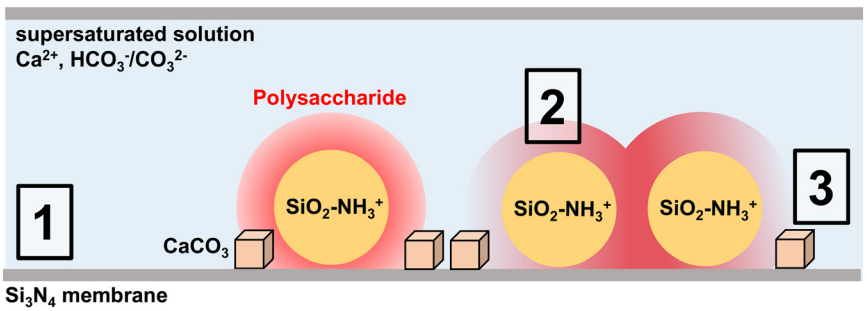

Fig. 6 Cross-section view of the fluid *in situ* TEM cell illustrating $CaCO_3$ nucleation adjacent to polysaccharides (red) on aminated silica nanoparticles (yellow). Boxes highlight three interfaces: (1) the Si_3N_4 membrane–solution interface; (2) polysaccharide–solution interface (coated silica nanoparticles); and (3) polysaccharide-coated nanoparticle–Si_3N_4 membrane–solution interface. In the chitosan and heparin systems, preferential nucleation at the polysaccharide–membrane–solution interface leads to the formation of $CaCO_3$ particles in a ring pattern around the coated nanoparticle. See the text for discussion.

charge distributions and hydrogen bonding.[35,68] For example, high charge polymers, like heparin, are expected to behave rigidly, leading to more water and ion structures, while low charge polymers, like chitosan, are more flexible.[30–32] Few particles in the TEM images formed in the region overlapping the SiO_2 nanoparticles (*e.g.*, Fig. 2C–F), suggesting that little nucleation took place at this interface.

Interface 3: Polysaccharide-coated nanoparticle–Si_3N_4 membrane–solution. This interface describes the three-way contact of the Si_3N_4 membrane (hydrophobic), the polysaccharide-coated nanoparticles (hydrophilic) and the bulk solution. TEM images of crystal nucleation in this environment would project as rings around the polysaccharide coatings on the membrane (Fig. 6, interface 3). Fig. 2D and F indeed show $CaCO_3$ crystallites forming in distinctive ring patterns. A probable explanation is a synergetic interaction of the three phases to favor heterogeneous nucleation. Cooperative interactions between carboxyl and sulfate groups are observed to promote $CaCO_3$ nucleation,[1] and a previous study of silica formation shows that nucleation preferentially occurs at the intersection of carboxyl and amine groups.[69] The activity of cooperative functional groups may arise from a locally low γ_{net} value relative to the polysaccharide–solution interface and a high frequency of nucleation events, perhaps by disrupting the water structure. The physical result is an enhanced rate of nucleation relative to the control and the formation of more uniformly sized $CaCO_3$ crystals that are approximately equidistant from (or patterned around) the polysaccharide-coated nanoparticles (Fig. 2D and F).

Conclusions

The findings from this *in situ* experimental study show that polysaccharide–water interfaces promote $CaCO_3$ nucleation when compared to the aminated SiO_2 nanoparticle control. We were unable to resolve detailed spatial relationships between the interfacial structure and crystal placement, but the measurements indicate that the number and position of the resulting crystals is likely related to polysaccharide-specific properties near the solution-interphase region. Heparin and chitosan present differences in net charge to the solution environment, and heparin is the most effective at controlling the placement and abundance of $CaCO_3$ crystallites. This result is consistent with heparin's larger effective persistence length that stabilizes ion-rich regions.

For both macromolecules, chitosan and heparin, heterogeneous nucleation is most-favored at the polysaccharide–TEM Si_3N_4 membrane contact, possibly through an additional influence of the TEM membrane on interfacial energy, ion concentration, and/or kinetic factors. The properties of the polysaccharides—through their interactions with local waters of solvation in these disrupted settings—directly influence where $CaCO_3$ nucleation occurs. The charged interface of the amine-functionalized silica nps leads to surrounding 'clouds' of high ion concentration, but this environment does not appear to have a structuring influence on the placement of $CaCO_3$ nuclei or the resulting crystal size relative to our observations for the polysaccharide interfaces. Thus, the evidence suggests that $CaCO_3$ nucleation in the control system is best described as a homogeneous process. The findings reiterate the need for a stronger mechanistic understanding of how the functional groups influence local polysaccharide properties and structuring to control the timing and placement of crystal nuclei during mineralization.

Author contributions

B. M. K., B. J., Y. B., J. J. D. Y., and P. M. D. designed the research; B. M. K., B. J., and Y. B. performed the research; B. M. K., B. J., Y. B., J. J. D. Y., and P. M. D. analyzed the data; and B. M. K., J. J. D. Y., and P. M. D. wrote the paper.

Conflicts of interest

There are no conflicts of interest to declare.

Data availability

Data for this article, including TEM images and $CaCO_3$ particle analysis, are available at Open Science Framework (OSF) at https://doi.org/10.17605/OSF.IO/KHJX6. Supplementary information (SI): which includes ATR data of polysaccharide coated nanoparticles, a schematic of the TEM setup, SAED pattern and *ex situ* images, TEM images for three heparin experiments, and reported measurments of calcite nucleation kinetics. Supplementary experiments using different solution conditions (crosslinked polysaccharides (no nanoparticles) and high ionic strength (IS = 0.6 M)) are also included in the SI. See DOI: https://doi.org/10.1039/d6ce00012f.

Acknowledgements

This material is based on the work supported by the U.S. Department of Energy, Office of Science, Office of Basic Energy Sciences, Geosciences program, with material preparation performed at Virginia Tech under Award Number DE FG02-00ER15112 (to P. M. D.) and *in situ* TEM performed at Pacific Northwest National Laboratory (PNNL) (to J. J. D. Y.) under FWP 56674. TEM experiments were performed on a project award (60753) from the Environmental Molecular Sciences Laboratory (EMSL), a DOE Office of Science User Facility sponsored by the Biological and Environmental Research program under Contract No. DE-AC05-76RL01830. PNNL is a multiprogram national laboratory operated for the DOE by Battelle Memorial Institute under Contract DE-AC05-76RL01830. We thank Alan Esker and Kevin Edgar for valuable discussions of polysaccharide behavior in aqueous solution.

References

1 L. Addadi, J. Moradian, E. Shay, N. G. Maroudas and S. Weiner, *Proc. Natl. Acad. Sci. U. S. A.*, 1987, **84**, 2732–2736.
2 L. Addadi, D. Joester, F. Nudelman and S. Weiner, *Chem. – Eur. J.*, 2006, **12**, 981–987.
3 R. Fried and Y. Mastai, *J. Cryst. Growth*, 2012, **338**, 147–151.
4 A. Gal, R. Wirth, Z. Barkay, N. Eliaz, A. Scheffel and D. Faivre, *Chem. Commun.*, 2017, **53**, 7740–7743.
5 H. Pyles, S. Zhang, J. J. De Yoreo and D. Baker, *Nature*, 2019, **571**, 251–256.
6 S. E. Gleeson, S. Kim, T. Yu, M. Marcolongo and C. Y. Li, *ACS Appl. Bio Mater.*, 2022, **5**, 4493–4503.
7 H. A. Lowenstam and S. Weiner, *On Biomineralization*, Oxford University Press, 1989.
8 J. L. Arias, A. Neira-Carrillo, J. I. Arias, C. Escobar, M. Bodero, M. David and M. S. Fernandez, *J. Mater. Chem.*, 2004, **14**, 2154–2160.
9 D. Raabe, C. Sachs and P. Romano, *Acta Mater.*, 2005, **53**, 4281–4292.
10 J. L. Arias and M. S. Fernandez, *Chem. Rev.*, 2008, **108**, 4475–4482.
11 A. Gal, R. Wirth, J. Kopka, P. Fratzl, D. Faivre and A. Scheffel, *Science*, 2016, **353**, 590–593.
12 J. L. Huang, Y. J. Liu, C. Liu, L. P. Xie and R. Q. Zhang, *Int. J. Biol. Macromol.*, 2021, **189**, 641–648.
13 B. M. Knight, K. J. Edgar, J. J. De Yoreo and P. M. Dove, *Biomacromolecules*, 2023, **24**, 1078–1102.
14 A. J. Giuffre, L. M. Hamm, N. Han, J. J. De Yoreo and P. M. Dove, *Proc. Natl. Acad. Sci. U. S. A.*, 2013, **110**, 9261–9266.
15 B. M. Knight, R. Mondal, N. Han, N. F. Pietra, B. A. Hall, K. J. Edgar, V. Vaissier Welborn, L. A. Madsen, J. J. De Yoreo and P. M. Dove, *Cryst. Growth Des.*, 2024, **24**, 6338–6353.
16 H. J. Li, D. Yan, H. Q. Cai, H. B. Yi, X. B. Min and F. F. Xia, *Phys. Chem. Chem. Phys.*, 2017, **19**, 11390–11403.
17 X. W. Wang, D. Toroz, S. Kim, S. L. Clegg, G. S. Park and D. Di Tommaso, *Phys. Chem. Chem. Phys.*, 2020, **22**, 16301–16313.
18 R. G. Alberstein, J. L. Prelesnik, E. Nakouzi, S. Zhang, J. J. De Yoreo, J. Pfaendtner, F. A. Tezcan and C. J. Mundy, *J. Phys. Chem. Lett.*, 2023, **14**, 80–87.
19 J.-N. Boyn and E. A. Carter, *J. Am. Chem. Soc.*, 2023, **145**, 20462–20472.
20 J. N. Boyn and E. A. Carter, *J. Phys. Chem. B*, 2023, **127**, 10824–10832.
21 F. A. Davila-Hernandez, B. Jin, H. Pyles, S. Zhang, Z. Wang, T. F. Huddy, A. K. Bera, A. Kang, C. L. Chen, J. J. De Yoreo and D. Baker, *Nat. Commun.*, 2023, **14**, 8191.
22 H. Söngen, S. J. Schlegel, Y. Morais Jaques, J. Tracey, S. Hosseinpour, D. Hwang, R. Bechstein, M. Bonn, A. S. Foster, A. Kühnle and E. H. G. Backus, *J. Phys. Chem. Lett.*, 2021, **12**, 7605–7611.
23 Y. W. Cheng, J. H. Tao, G. M. Zhu, J. A. Soltis, B. A. Legg, E. Nakouzi, J. J. De Yoreo, M. L. Sushko and J. Liu, *Nanoscale*, 2018, **10**, 11907–11912.
24 G. M. Zhu, M. L. Sushko, J. S. Loring, B. A. Legg, M. Song, J. A. Soltis, X. P. Huang, K. M. Rosso and J. J. De Yoreo, *Nature*, 2021, **590**, 416–422.
25 C. Zeng, C. Vitale-Sullivan and X. Ma, *Minerals*, 2017, **7**, 158.
26 S. Pu, C. Gong and A. W. Robertson, *R. Soc. Open Sci.*, 2020, **7**, 191204.
27 M. V. Shapovalov and R. L. Dunbrack Jr, *Proteins: Struct., Funct., Bioinf.*, 2007, **66**, 279–303.
28 M. Kurudirek and T. Onaran, *Radiat. Phys. Chem.*, 2015, **112**, 125–138.
29 B. Cuevas-Zuviría and L. F. Pacios, *J. Chem. Inf. Model.*, 2020, **60**, 3831–3842.
30 P. J. Flory, *Principles of polymer chemistry*, Cornell University Press, Ithaca, N.Y., 1953.
31 G. A. Morris, J. Castile, A. Smith, G. G. Adams and S. E. Harding, *Carbohydr. Polym.*, 2009, **76**, 616–621.
32 G. Pavlov, S. Finet, K. Tatarenko, E. Korneeva and C. Ebel, *Eur. Biophys. J.*, 2003, **32**, 437–449.
33 H. C. Brown, D. H. McDaniel and O. HÄFliger, in *Determination of Organic Structures by Physical Methods*, ed. E. A. Braude and F. C. Nachod, Academic Press, 1955, pp. 567–662.
34 T. Schiestel, H. Brunner and G. E. M. Tovar, *J. Nanosci. Nanotechnol.*, 2004, **4**, 504–511.
35 M. Rinaudo, *Prog. Polym. Sci.*, 2006, **31**, 603–632.
36 Q. Wang, X. Chen, N. Liu, S. Wang, C. Liu, X. Meng and C.-G. Liu, *Carbohydr. Polym.*, 2006, **65**, 194–201.
37 B. M. Knight, C. M. B. Gallagher, M. D. Schulz, K. J. Edgar, C. D. McNaul, C. A. McCutchin and P. M. Dove, *Proc. Natl. Acad. Sci. U. S. A.*, 2025, **122**, e2504348122.
38 J. W. Park and B. Chakrabarti, *Biochem. Biophys. Res. Commun.*, 1977, **78**, 604–608.
39 H. M. Wang, D. Loganathan and R. J. Linhardt, *Biochem. J.*, 1991, **278**, 689–695.
40 V. R. Sinha, A. K. Singla, S. Wadhawan, R. Kaushik, R. Kumria, K. Bansal and S. Dhawan, *Int. J. Pharm.*, 2004, **274**, 1–33.
41 N. Reddy, R. Reddy and Q. R. Jiang, *Trends Biotechnol.*, 2015, **33**, 362–369.
42 L. N. Plummer and E. Busenberg, *Geochim. Cosmochim. Acta*, 1982, **46**, 1011–1040.
43 C. M. Bethke, *The Geochemist's Workbench*, Release 3.0 edn, 1998.
44 C. A. Schneider, W. S. Rasband and K. W. Eliceiri, *Nat. Methods*, 2012, **9**, 671–675.
45 B. Jin, Y. Chen, H. Pyles, M. Baer, B. Legg, Z. Wang, N. Washton, K. Mueller, D. Baker, G. Schenter, C. Mundy and J. De Yoreo, *Nat. Mater.*, 2025, **24**, 125–132.
46 Z. Liu, Z. Zhang, Z. Wang, B. Jin, D. Li, J. Tao, R. Tang and J. De Yoreo, *Proc. Natl. Acad. Sci. U. S. A.*, 2020, **117**, 3397–3404.
47 P. Smeets, A. Finney, W. Habraken, F. Nudelman, H. Friedrich, J. Laven, J. De Yoreo, P. Rodger and N. Sommerdijk, *Proc. Natl. Acad. Sci. U. S. A.*, 2017, **114**, E7882–E7890.
48 Q. Hu, M. H. Nielsen, C. L. Freeman, L. M. Hamm, J. Tao, J. R. I. Lee, T. Y. J. Han, U. Becker, J. H. Harding, P. M.

Dove and J. J. De Yoreo, *Faraday Discuss.*, 2012, **159**, 509–523.
49 P. Liang, Y. Zhao, Q. Shen, D. J. Wang and D. F. Xu, *J. Cryst. Growth*, 2004, **261**, 571–576.
50 Y. P. Huang, Q. Shen, W. P. Sui, M. L. Guo, Y. Zhao, D. J. Wang and D. F. Xu, *Colloid Polym. Sci.*, 2007, **285**, 641–647.
51 M. E. Fortuna, E. Ungureanu and C. D. Jitareanu, *Materials*, 2021, **14**, 3336.
52 J. N. Israelachvili, *Intermolecular and Surface Forces*, Elsevier, 3rd edn, 2011.
53 C. G. Sinn, R. Dimova and M. Antonietti, *Macromolecules*, 2004, **37**, 3444–3450.
54 M. Kellermeier, P. Raiteri, J. K. Berg, A. Kempter, J. D. Gale and D. Gebauer, *ChemPhysChem*, 2016, **17**, 3535–3541.
55 V. V. Welborn, W. R. Archer and M. D. Schulz, *J. Chem. Inf. Model.*, 2023, **63**, 2030–2036.
56 D. Martin-Jimenez, E. Chacon, P. Tarazona and R. Garcia, *Nat. Commun.*, 2016, **7**, 12164.
57 H. Söngen, R. Bechstein and A. Kühnle, *J. Phys.: Condens. Matter*, 2017, **29**, 274001.
58 E. Nakouzi, S. Kerisit, B. A. Legg, S. Yadav, D. Li, A. G. Stack, C. J. Mundy, J. Chun, G. K. Schenter and J. J. De Yoreo, *J. Phys. Chem. C*, 2023, **127**, 2741–2752.
59 M. Zhang, B. A. Legg, B. A. Helfrecht, Y. Zhang, S. Tan, Y. Xia, R. K. Yodong, M. Iepure, V. Prabhakaran, P. J. Pauzauskie, Y. Min, C. J. Mundy and J. J. De Yoreo, *Nat. Mater.*, 2026, **25**, 487–494.
60 L. F. Alexander and N. Radacsi, *CrystEngComm*, 2019, **21**, 5014–5031.
61 A. Chernov, *Phys.-Usp.*, 1961, **4**, 116–148.
62 A. Chernov, *Modern Crystallography III: Crystal Growth*, Springer, Berlin, 1984.
63 C. A. DiTusa, T. Christensen, K. A. McCall, C. A. Fierke and E. J. Toone, *Biochemistry*, 2001, **40**, 5338–5344.
64 J. J. De Yoreo and P. G. Vekilov, *Rev. Mineral. Geochem.*, 2003, **54**, 57–93.
65 D. N. Petsev, K. Chen, O. Gliko and P. G. Vekilov, *Proc. Natl. Acad. Sci. U. S. A.*, 2003, **100**, 792–796.
66 B. A. Khorramian and S. S. Stivala, *Arch. Biochem. Biophys.*, 1986, **247**, 384–392.
67 D. Kashchiev and G. M. van Rosmalen, *Cryst. Res. Technol.*, 2003, **38**, 555–574.
68 D. Laage, T. Elsaesser and J. T. Hynes, *Chem. Rev.*, 2017, **117**, 10694–10725.
69 A. F. Wallace, J. J. DeYoreo and P. M. Dove, *J. Am. Chem. Soc.*, 2009, **131**, 5244–5250.